Journal of Solid State Chemistry **156,** 168–180 (2001)
doi:10.1006/jssc.2000.8978, available online at http://www.idealibrary.com on IDEAL®

$Bi_{1-x}Cr_xO_{1.5+1.5x}$, $0.05 \leq x \leq 0.15$: A New High-Temperature Solid Solution with a Three-Dimensional Incommensurate Modulation

S. Esmaeilzadeh,*,[1] S. Lundgren,* U. Hålenius,† and J. Grins

*Department of Inorganic Chemistry, Arrhenius Laboratory, Stockholm University, SE-106 91 Stockholm, Sweden; and †Department of Mineralogy, Swedish Muséum of Natural History, Box 50007, SE-104 05 Stockholm, Sweden

Received June 14, 2000; in revised form August 23, 2000; accepted October 3, 2000; published online December 21, 2000

A new metastable solid solution $Bi_{1-x}Cr_xO_{1.5+1.5x}$ with $0.05 \leq x \leq 0.15$ was synthesized by quenching Bi–Cr–O melts and structurally investigated using electron microscopy and X-ray diffraction. The oxidation state of Cr was determined to be + VI by thermogravimetry, optical spectroscopy, and magnetic measurements. Infrared spectra indicate for $x = 0.05$ isolated CrO_4^{2-} tetrahedra and also smaller fractions of $Cr_2O_7^{2-}$ units. The phase exhibits an average structure of the $Fm\bar{3}m$ fluorite type and a 3D incommensurate modulation, with wave vectors $q_1 = [\alpha, 0, 0]^*$, $q_2 = [0, \alpha, 0]^*$, $q_3 = [0, 0, \alpha]^*$, $a = 5.6025(3)$ Å, and $\alpha = 0.2866(2)$ for $x = 0.15$, and with the 3 + 3D superspace group symmetry $P{:}Fm\bar{3}m{:}Fm\bar{3}m$. Atomic modulation functions and periodic nodal surfaces were deduced for observed satellite reflections and a commensurate structure model derived for $x = 0.05$. The modulated structure was compared with that of $Bi_{0.78}Nb_{0.22}O_{1.72}$, with symmetry $P{:}Fm\bar{3}m{:}Fd\bar{3}m$. © 2001 Academic Press

INTRODUCTION

The high-temperature modification of bismuth oxide, δ-Bi_2O_3, is one of the best oxygen ion conductors known (1). Its structure is related to that of cubic fluorite and the phase is stable above 729°C up to the melting point (840°C). The small temperature range within which it is stable and the inability to quench the phase to room temperature has complicated structural investigations and prohibited usage of it as a solid electrolyte in commercial devices.

Bismuth oxide-based compounds with fluorite type structures can be stabilized in two ways, either by adding higher valent cations, as Nb^{5+} or W^{6+} (2–4), or larger cations, as Y^{3+} or Ho^{3+} (5, 6). In the first case the structure is stabilized by an increase in the number of O atoms according to $Bi_{2-x}M_x^{y+}O_{(3+x(y-3)/2)}$. It is noteworthy here that ternary bismuth-rich compounds with fluorite-related structures in the systems Bi–M–O (M = V, Nb, Ta, Mo, W) display a variety of superstructures and/or commensurate and incommensurate modulations (2–4, 7–9). In the second case, the larger cations stabilize the cubic coordination of O atoms around the cations in the fluorite structure. In contrast to, e.g., the Bi–W–O and Bi–Mo–O systems, very few structural investigations have been made of bismuth-rich Bi–Cr oxides, with the notable exception of a single-crystal XRD study of $Bi_{14}CrO_{24}$ (10), with a structure related to that of β-Bi_2O_3.

There are at present only seven compounds reported that possess three-plus-three-dimensional (3 + 3D) structures. As many as four of these are Bi_2O_3-based: $Bi_{1-x}Nb_xO_{1.5+x}$ ($0.06 < x < 0.23$) (2, 3, 11) and $Bi_{1-x}Ta_xO_{1.5+x}$ ($0.1 < x < 0.25$) (3), both with symmetry $P{:}Fm\bar{3}m{:}Fd\bar{3}m$, $Bi_{1-x}Mo_xO_{1.5+1.5x}$ with $x = 0.16$ and symmetry $P{:}Fm\bar{3}m{:}Fm\bar{3}m$ (7), and $BaBi_3O_{5.5}$ (12, 13) with symmetry $P{:}Im\bar{3}m{:}Im\bar{3}m$. The remaining three are: wüstite $Fe_{1-x}O$ (14) with symmetry $P{:}Fm\bar{3}m{:}Pm\bar{3}m$, $V_6Ni_{16}Si_7$ (15) with symmetry $N{:}Im\bar{3}m{:}Fm\bar{3}m$, and Cu_9BiS_6 (16) with symmetry $P{:}Fm\bar{3}m{:}Fm\bar{3}m$.

EXPERIMENTAL

Single-phase samples of $Bi_{1-x}Cr_xO_{1.5+1.5x}$ with $x = 0.05$, 0.10, and 0.15 were prepared using mixtures of Bi_2O_3 and Cr_2O_3 as starting materials. The mixtures were ground, pelletized, and fired, at 850°C for $x = 0.05$ and at 950°C for $x = 0.10$ and 0.15, in Pt crucibles in air for 5 min. The samples were found to be molten at these temperatures. The melts were quenched to room temperature by immersing into water, yielding transparent and homogenous products with an intense red color. The compound $Bi_{0.78}Nb_{0.22}O_{1.72}$ was synthesized by cooling a Bi–Nb–O melt with nominal composition from 1150 to 800°C during 20 min and then quenching the sample.

Metal compositions were determined by energy dispersive X-ray (EDX) microanalysis, using a LINK AN10000

[1]To whom correspondence should be addressed. E-mail: zaida@inorg.su.se.

0022-4596/01 $35.00

system mounted in a JEOL JSM-820 scanning electron microscope (SEM).

Electron diffraction patterns were collected in a JEOL 2000FX transmission electron microscope operating at 200 kV. A JEOL 3010 electron microscope, with an acceleration voltage of 300 kV and optimal resolution of 1.7 Å, was used for high-resolution electron microscopy (HREM). The investigated specimens were crushed, dispersed in butanol, and the dispersions were transferred onto holey carbon-coated copper grids. The image processing of the HREM images were performed using the computer program CRISP (17)

Unit cell parameters and q-vector lengths were determined from Guinier-Hägg films, using CuKα_1 radiation and Si as internal standard. The data were evaluated using a film scanner system (18). A STOE diffractometer with an image plate detector system and MoKα radiation was used for the single-crystal XRD study.

A Perkin Elmer TGA7 thermogravimetric analyzer was used for determining oxygen contents and the oxidation state of Cr by heating mixtures of Bi_2O_3 and Cr_2O_3, with ratios 95:5, 90:10, and 85:15 in Pt crucibles in air at a rate of 10°C/min.

A weak-field *ac* susceptometer (Lake Shore 7130) was used for magnetic measurements in the temperature range 11–300 K, using a magnetic field of 500 A m^{-1} and a frequency of 500 Hz.

For optical absorption measurements, crystals of high optical quality, i.e., showing large areas devoid of inclusions and also displaying indisputable optical isotropy, were selected. The crystals were embedded in a thermoplastic resin and subsequent to resin hardening they were ground and polished on two parallel surfaces. The resulting thickness of individual absorbers was in the range 15–19 μm, as determined by means of a digital micrometer. Optical absorption spectra of the prepared absorbers were recorded in the divisible spectral range by a Zeiss MPM 800 microscope–spectrophotometer at ambient temperature. The spectrometer was equipped with a 75-W xenon arc lamp as a light source, concave holographic gratings as a monochromator, and a photomultiplier detector. The beam of unpolarized light was focused on the absorbers using Zeiss 10× Ultrafluar lenses as condenser and objective. In all measurements, the spectral slit width was set at 5 nm and data was collected in 5-nm steps during three cycles. Air served as a reference medium and the circular measuring spot equaled 30 μm in diameter.

Infrared absorption spectra were recorded with a Bruker IFS-55 FT-IR spectrometer.

RESULTS

Phase Analysis

The metal compositions for the samples were determined from 20 EDX point analysis on single-crystal surfaces. The analyses results were, within an experimental error of ca. 1 at. %, in good agreement with the nominal compositions.

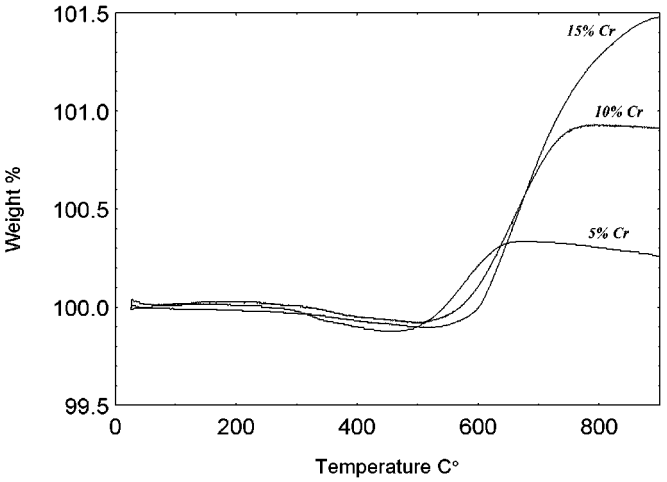

FIG. 1. TG curves for Bi_2O_3:Cr_2O_3 mixtures heated in air.

Thermogravimetric analyses showed that upon heating mixtures of Bi_2O_3 and Cr_2O_3 in air, an irreversible increase in weight begins at 450–500°C and reaches, depending on the Cr concentration, a plateau at 650 to 900°C, as shown in Fig. 1. The weight increase corresponds well to that of a complete oxidation of Cr^{3+} to Cr^{6+}. This oxidative behavior is quite unusual for Cr-containing materials in air, at normal pressure, and these high temperatures. Magnetic susceptibility measurements confirmed an oxidation state of + VI for Cr, as no or only very weak paramagnetic signals were observed.

Electron Diffraction

Electron diffraction patterns (EDPs) were recorded to study the modulation vectors and to determine the symmetry. For comparison, EDPs were also collected for the Bi–Nb phase $Bi_{0.78}Nb_{0.22}O_{1.72}$. The two crystallographic directions mainly studied were ⟨110⟩ and ⟨100⟩ (see Fig. 2a–2f).

For both phases the strongest reflections in the ⟨110⟩ zone axis form a centered pattern from the average structure with $Fm\bar{3}m$ symmetry. In addition there are a considerable number of satellite reflections. They are found at approximately the same positions for the Bi–Cr and Bi–Nb phases but with quite different intensities. The strongest are found in ⟨111⟩* directions and the appropriate way to index them, using the highest possible symmetry, is to use a 3 + 3D index system with six indices *hklmnp*. The q-vector lengths are shorter for the Bi–Cr phase, ≈ 0.29 in units of the reciprocal unit cell parameter, than for the Bi–Nb phase, ≈ 0.36. For the Bi–Cr phase the only systematic extinction observed for the satellite reflections was $F_{\langle hklmnp\rangle} = 0$ unless

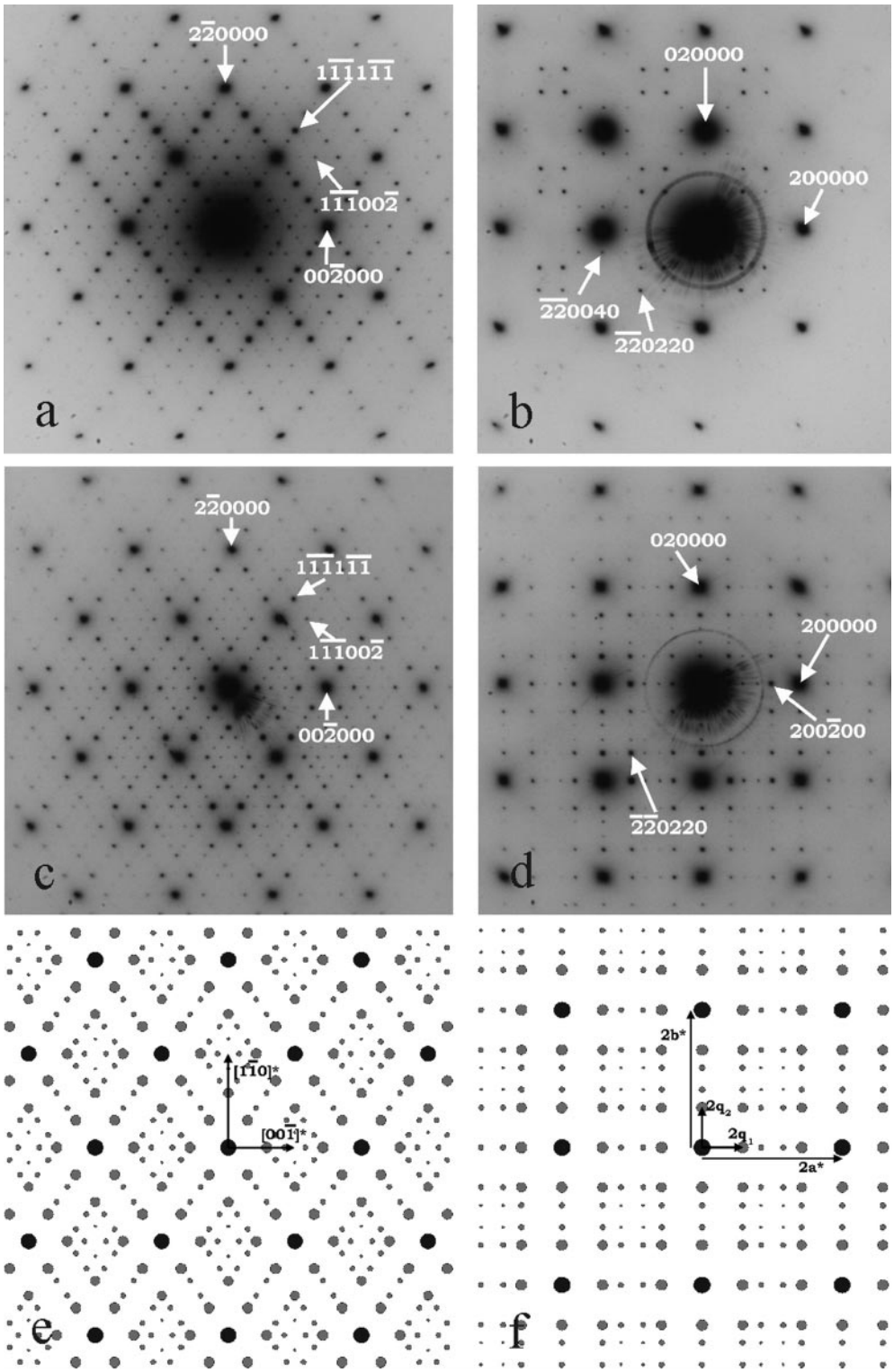

FIG. 2. (a) ⟨110⟩ and (b) ⟨100⟩ zone EDPs of $Bi_{0.78}Nb_{0.22}O_{1.72}$; (c) ⟨110⟩ and (d) ⟨100⟩ zone EDPs of $Bi_{0.85}Cr_{0.15}O_{1.73}$. Schematic (e) ⟨110⟩ and (f) ⟨100⟩ zone diffraction patterns of $Bi_{0.85}Cr_{0.15}O_{1.73}$.

$m + n = 2j$, $m + p = 2j$, and $n + p = 2j$. Together with the average $Fm\bar{3}m$ symmetry this implies a 3 + 3D superspace group symmetry $P{:}Fm\bar{3}m{:}Fm\bar{3}m$. The symmetry elements of this superspace group are listed in Table 1, where v_1, v_2, and v_3 are three additional fractional indices of the 6D unit cell defined as $v_n = \mathbf{q}_n \cdot \mathbf{r}$ and $\mathbf{r} = \mathbf{a} \cdot x + \mathbf{b} \cdot y + \mathbf{c} \cdot z$.

TABLE 1
Symmetry Elements of the 3 + 3D Superspace Group $P{:}Fm\bar{3}m{:}Fm\bar{3}m$

x	y	z	v_1	v_2	v_3	The identity operator
$x+\frac{1}{2}$	$y+\frac{1}{2}$	z	v_1	v_2	v_3	Face centering of the average structure
x	$y+\frac{1}{2}$	$z+\frac{1}{2}$	v_1	v_2	v_3	Face centering of the average structure
x	y	z	$v_1+\frac{1}{2}$	$v_2+\frac{1}{2}$	v_3	Face centering of the 3D modulation
x	y	z	v_1	$v_2+\frac{1}{2}$	$v_3+\frac{1}{2}$	Face centering of the 3D modulation
$-x$	y	z	$-v_1$	v_2	v_3	σ_x, Mirror plane perpendicular to the x axis
$-x$	$-y$	$-z$	$-v_1$	$-v_2$	$-v_3$	I, The center of symmetry
y	x	z	v_2	v_1	v_3	Negative permutation
z	x	y	v_3	v_1	v_2	Positive permutation

The symmetry for $Bi_{1-x}Nb_xO_{1.5+x}$ with $0.06 < x < 0.23$ has previously been deduced to be $P{:}Fm\bar{3}m{:}Fd\bar{3}m$ (3, 11), i.e., to have the additional extinction condition $F_{\langle hklmn0\rangle} = 0$ unless $m + n = 4j$. Reflections of the type $hkl200$ should then have zero intensity due to the presence of a d-glide for the modulations. Such reflections were in fact visible in $\langle 110\rangle$ zone patterns for the Bi-Nb phase, but in this zone they originate from strong multiple scattering and they were not present in $\langle 001\rangle$ zone patterns, thus confirming the existence of a d-glide for the modulation for $Bi_{0.78}Nb_{0.22}O_{1.72}$.

The $\langle 001\rangle$ zone patterns clearly demonstrate the difference in the symmetry for $Bi_{0.85}Cr_{0.15}O_{1.73}$ and $Bi_{0.78}Nb_{0.22}O_{1.72}$. The EDP for the Bi–Nb phase contains satellite reflections of the type $hkl220$ and $hkl400$, while for the Bi–Cr phase there are in addition relatively strong $hkl200$ and $hkl220$, and weaker $hkl400$ and $hkl420$, satellites. The major differences are thus that (i) the modulation vector is shorter for the Bi–Cr phase, (ii) there is no d-glide for the modulation in the Bi–Cr phase, and (iii) higher order satellites are present for the Bi–Cr phase, indicating sharper atomic modulation functions.

High-Resolution Electron Microscopy

HREM is a very useful tool for studying incommensurately modulated structures. In addition to that much smaller crystals can be used than in conventional diffraction techniques, the perhaps greatest advantage is that a projection of the investigated structure is obtained. This can be helpful during a structure determination and even more importantly provide an understanding of higher dimensional crystallography and structures in a real 3D space. The symmetry of a specific projection can be used in image processing and also for a determination of modulations.

In the present case, both the 2D plane group for the average structure and the 2 + 2D superspace group symmetry for the modulated structure are important. The symmetry of the $\langle 110\rangle$ projection of the average structure is *Cmm*. The 2D modulation must then have the same *mm* point-group symmetry. The centering condition $F_{\langle hkmn\rangle} = 0$ unless $m + n = 2j$ is also easily seen in the diffraction pattern. The 2 + 2D superspace group can then be derived to be $P{:}Cmm{:}Cmm$ with unit cell parameters $a \approx 5.6$ and $b \approx \sqrt{2} \times 5.6$ Å and q vectors $\mathbf{q}_1 = [\alpha, 0]^*$ and $\mathbf{q}_2 = [0, \alpha]^*$ with $\alpha \approx 0.29$. It should be noted that this superspace group, written in a nonstandard setting, is used for an easier understanding of the relation to the 3 + 3D symmetry. The superspace group $P{:}Cmm{:}Pmm$ with $\mathbf{q}_1 = [\alpha, \beta]$ and $\mathbf{q}_2 = [\alpha, -\beta]$ should be used in other cases. An important and useful symmetry constraint here is also that the plane group is centrosymmetric, which follows from the *mm* symmetry. The centrosymmetry implies that a corresponding calculated HREM image can be constructed using only cosine functions, in directions and with periodicities defined by the unit cell parameters and the q-vectors. The amplitudes of the cosine functions can be derived from diffracted intensities and their phase shifts, 0° or 180° for a centrosymmetric pattern, extracted from Fourier transforms (FTs) of the HREM image. From a FT of a HREM image of a modulated structure the amplitudes and, more importantly, the phase shifts of both basic and satellite reflections can be estimated. By combining phase and amplitude information for Bragg peaks with symmetry constraints, noise in a HREM image can be removed and a clearer picture of the modulation obtained.

A HREM image of the Bi-Cr phase in the $\langle 110\rangle$ direction is shown in Fig. 3a and a FT of it in Fig. 3b. Amplitudes and phase shifts of different Bragg peaks were extracted from the latter and averaged with respect to the 2 + 2D superspace group symmetry. They are tabulated in Table 2. The frequencies of the reflections were then used for a Fourier synthesis of the noise-free image shown in Fig. 3c. The data in Table 2 are useful not only for image processing but, since the structure is cubic, they can also be used for a 3D analysis of the complete structure, including both basic and satellite reflections. In this way a probable 3 + 3D structure solution can be derived and illustrated in a way that is comprehensible for human 3D perception.

The HREM image shows that the structure contains a compositional modulation of the metals Bi^{3+}/Cr^{6+}. An accompanying compositional modulation of O atoms and

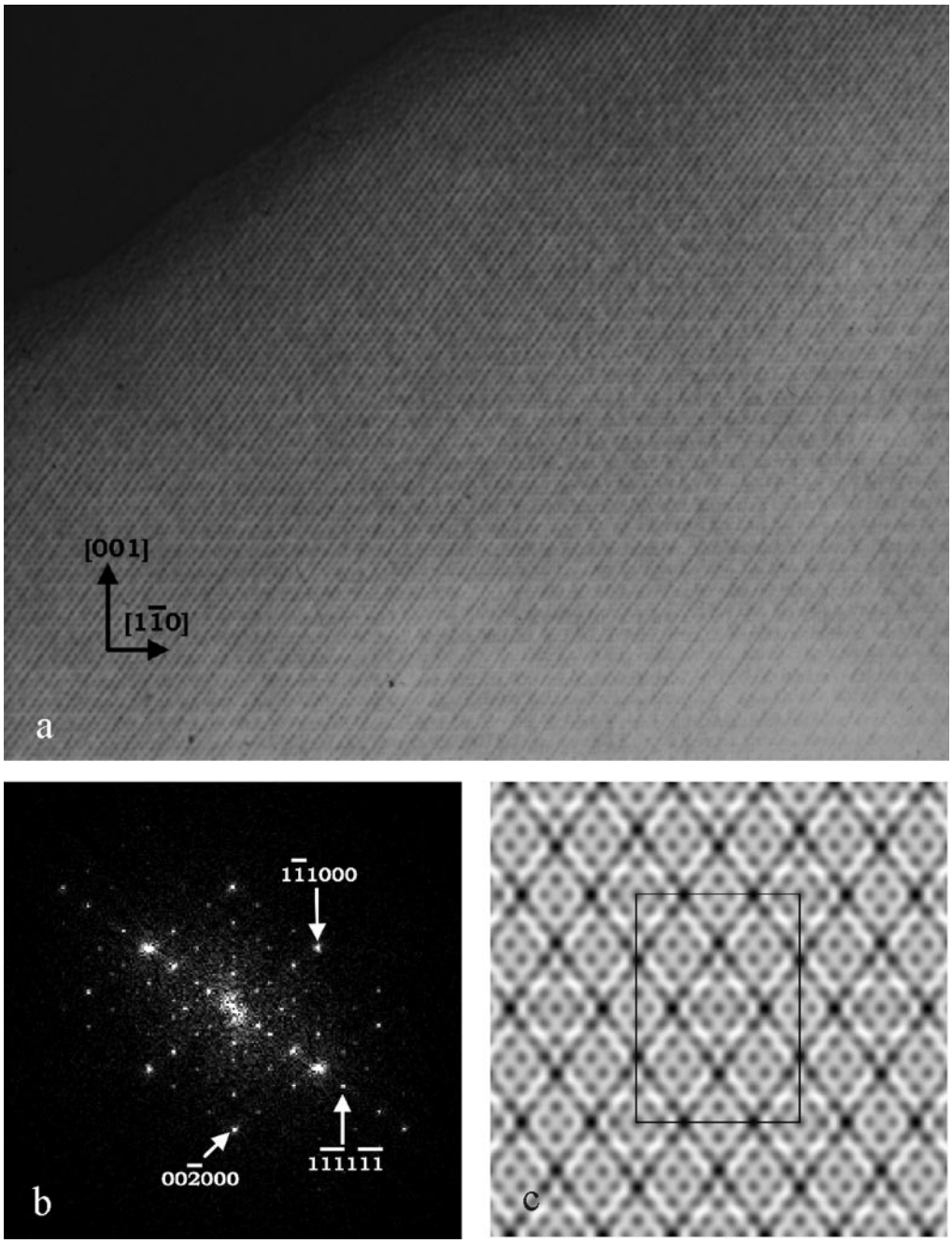

FIG. 3. (a) A HREM image of $Bi_{0.85}Cr_{0.15}O_{1.73}$ along $\langle 110 \rangle$, (b) the Fourier transform of the HREM image, and (c) a symmetry-corrected and Fourier-filtered image of a commensurate approximant with a 7×7 superstructure of the cubic fluorite unit cell.

vacancies is very probable, due to the difference in size and charge of Bi^{3+} and Cr^{6+} ions. The compositional modulations will also be paralleled by displacive modulations of a relaxation of the average structure. Much stronger local displacive modulations can also be seen in the HREM image.

Single-Crystal X-ray Diffraction

The average structure of $Bi_{0.85}Cr_{0.15}O_{1.73}$ was refined from single-crystal Mo$K\alpha$ XRD data to a weighted R value of 2.6%, in space group $Fm\bar{3}m$ and with $a = 5.6025(3)$ Å. A total number of 178 basic reflections were integrated, out

TABLE 2
Amplitude and Phase Shift of Selected ED Reflections

Indices	Amplitude	Averaged amplitude	Phase shift	Phase shift fixed to 0° or 180°
$1\bar{1}\bar{1}000$	10000	6564	−180	180
$1\bar{1}1000$	3129	6564	−179	180
002000	3106	3106	−153	180
$0001\bar{1}\bar{1}$	3387	2901	14	0
$0001\bar{1}1$	2414	2901	−41	0
$1\bar{1}\bar{1}\bar{1}11$	5170	3816	25	0
$1\bar{1}1\bar{1}1\bar{1}$	2462	3816	−84	0
$1\bar{1}\bar{1}222$	2063	1548	−176	180
$1\bar{1}1\bar{2}2\bar{2}$	1033	1548	−156	180
000002	2982	2982	159	180
$002002\bar{}$	993	993	−19	0
$002002\bar{}$	722	722	−131	180
$1\bar{1}\bar{1}\bar{1}13$	1115	1154	53	0
$1\bar{1}1\bar{1}1\bar{3}$	1193	1154	−117	0
$000\bar{2}\bar{2}0$	2937	2937	−176	180
$1\bar{1}\bar{1}002$	1410	868	−171	180
$1\bar{1}100\bar{2}$	326	868	−170	180
$1\bar{1}\bar{1}1\bar{1}\bar{1}$	1004	537	33	0
$1\bar{1}11\bar{1}1$	70	537	−67	0

of which 16 were unique. The cations, Bi^{3+} (85%) and Cr^{6+} (15%), were distributed on the 4(*a*) positions (0, 0, 0) and the O atoms on the 8(*c*) positions ($\frac{1}{4}$, $\frac{1}{4}$, $\frac{1}{4}$) with an occupancy of 86%. The two refined structural parameters were isotropic thermal displacement parameters for the metals, $U = 0.0658(5)\,Å^2$, and O atoms, $U = 0.142(7)\,Å^2$.

The large displacement parameter for the O atoms show that they are highly disordered, a common case for oxygen-deficient fluorite-type oxides. Fourier maps illustrating the O atom disorder are shown in Figs. 4a and 4b. They indicate moreover split positions for the O atoms, similar to those reported for δ-Bi_2O_3 (19) and the 3D modulated Bi–Nb oxide Bi_3NbO_7 (2). Note that 14% of the O atom sites are vacant in the structure of $Bi_{0.85}Cr_{0.15}O_{1.73}$.

X-Ray Powder Diffraction

Guinier-Hägg film data was used to determine cell parameters and *q*-vector lengths. As the satellite reflections were considerably weaker than the main ones, two films were recorded for each sample, one of them heavily overexposed, and their reflection intensities scaled. The powder pattern for $Bi_{0.95}Cr_{0.05}O_{1.58}$ contained in addition comparatively broad reflections from a tetragonal fluorite type phase, with an *I*-centred unit cell with $a = 3.8757(5)$ and $c = 5.662(2)$ Å and with an estimated amount of 10%. This is probably formed during the quenching, since a phase with a similar subcell, but better crystallized and with many more reflections, were found in samples with 5–10% Cr that were heat-treated at temperatures below 800°C. The samples of $Bi_{0.90}Cr_{0.10}O_{1.65}$, $Bi_{0.85}Cr_{0.15}O_{1.73}$, and $Bi_{0.878}Nb_{0.22}O_{1.72}$ were found to be monophasic.

The unit cell parameters, *a*, were first refined by linear least squares. The satellite reflection were then assigned indices by hand and approximate values for the *q*-vector lengths, α, found by a grid search. Refined values for *a* and

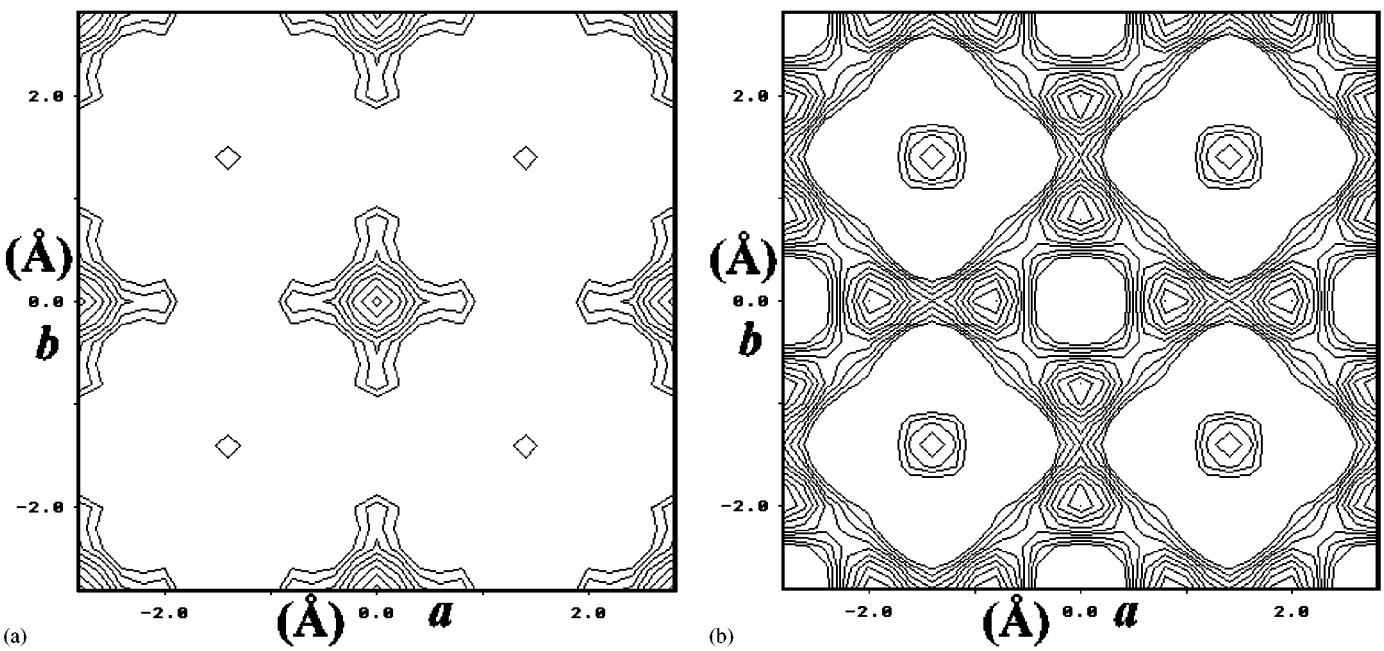

FIG. 4. (a) A Fourier map of the $Bi_{0.85}Cr_{0.15}O_{1.73}$ structure, centered on the O atom position, and (b) a difference Fourier map for the same section.

α were finally obtained by nonlinear least squares. Intensities for the satellite reflections were estimated using the program Winfit (20). Observed satellite reflections for the Cr-containing phases are given in Table 3 and for $Bi_{0.78}Nb_{0.22}O_{1.72}$ in Table 4. The majority of the satellite reflections are of the kind *hkl*111, in consistency with the ED data. The unit cell parameters for the Cr containing samples are smaller than that reported for pure δ-Bi_2O_3, $a = 5.6485(6)$ Å (21), and increase slightly with Cr content. For $Bi_{0.95}Cr_{0.05}O_{1.58}$ only one satellite reflection, 000111, was observable, corresponding to $\alpha = 0.307$. With increasing Cr content, the number and intensities of the satellite reflections increase and the α value decreases. The number $a \cdot \alpha$ shows a linear dependence on the nominal Cr concentration. The majority of satellite reflections observed for the Cr samples, and also the Nb-containing one, have the same indices as those observed for $Bi_{0.15}Mo_{0.85}O_{1.73}$ (7). This demonstrates a structural similarity for these phases, regardless of the significant difference in space group symmetry for the Bi–Nb phase.

TABLE 3
Powder X-ray Diffraction Patterns for $Bi_{1-x}Cr_xO_{1.5+1.5x}$ with $x = 0.05$, 0.10, and 0.15

	$Bi_{0.95}Cr_{0.05}O_{1.58}$ $a = 5.5867(3)$ Å $\alpha = 0.307$		$Bi_{0.90}Cr_{0.10}O_{1.65}$ $a = 5.5905(2)$ Å $\alpha = 0.2973(2)$			$Bi_{0.85}Cr_{0.15}O_{1.73}$ $a = 5.6025(3)$ Å $\alpha = 0.2866(2)$		
hklmnp	$2\theta_{obs}$	I/I_0(‰)	$2\theta_{obs}$	$\Delta 2\theta$	I/I_0(‰)	$2\theta_{obs}$	$\Delta 2\theta$	I/I_0(‰)
000111	8.400	7	8.133	0.000	18	7.803	−0.017	34
000200						9.046	0.014	4
000220			13.319	0.015	4	12.776	−0.016	13
111$\bar{1}\bar{1}\bar{1}$			19.279	−0.028	2	19.565	0.004	4
200$\bar{2}$20						24.392	−0.016	2
111$\bar{1}$11						26.004	0.024	10
111$\bar{2}$20			30.786	0.018	7	30.471	−0.014	17
111$\bar{1}$11			31.445	0.033	23	31.169	−0.002	21
111020						33.814	0.002	5
111111			36.093	0.022	2	35.657	−0.021	5
200111			37.495	−0.047	4	37.235	0.000	5
111220			39.705	−0.037	1			
220$\bar{2}\bar{0}\bar{2}$			40.571	0.009	3	40.595	0.007	7
220$\bar{1}\bar{1}$			46.635	−0.036	4	46.532	0.025	13
311$\bar{1}\bar{1}\bar{1}$						46.929	0.021	11
222$\bar{1}\bar{1}\bar{1}$			47.982	0.031	6	48.156	−0.006	5
311$\bar{2}$02						49.772	0.012	2
331$\bar{1}\bar{1}\bar{1}$			64.739	−0.012	5	64.897	−0.013	4
420$\bar{1}\bar{1}$1			68.519	−0.011	6	66.727	0.001	7

Note. Only satellite reflections are included and the intensities given are relative to the strongest, 111, fluorite reflection. $\Delta 2\theta = 2\theta_{obs} - 2\theta_{calc}$, $\lambda = 1.5406$ Å.

TABLE 4
Powder X-ray Diffraction Pattern for $Bi_{0.78}Nb_{0.22}O_{1.72}$

hklmnp	$2\theta_{obs}$	$\Delta 2\theta$	I/I_0(‰)
000111	10.783	0.030	8
111$\bar{2}\bar{2}$0	17.040	−0.003	1
000220	17.643	0.034	1
111$\bar{1}\bar{1}$1	26.647	0.012	5
200$\bar{1}\bar{1}\bar{1}$	27.805	0.020	15
111$\bar{1}$11	33.614	0.012	16
220$\bar{1}\bar{1}\bar{1}$	38.099	0.002	4
200111	40.309	0.014	4
220$\bar{2}$02	40.739	0.000	2
111022	44.597	0.007	1
311$\bar{1}\bar{1}\bar{1}$	45.707	0.008	3
222$\bar{1}\bar{1}\bar{1}$	46.640	0.030	9
200$\bar{2}\bar{2}$0	47.738	−0.004	3
220$\bar{1}$1$\bar{1}$	48.320	0.003	8
311$\bar{1}\bar{1}$1	50.397	−0.001	3
220111	57.115	0.005	3
3111$\bar{1}\bar{1}$	58.950	−0.021	1
31111$\bar{1}$	62.980	0.012	1
22211$\bar{1}$	63.535	−0.023	1
311111	66.813	−0.015	2
331$\bar{1}$1$\bar{1}$	74.956	−0.033	5
4201$\bar{1}$1	82.663	0.008	1
400202	85.735	−0.002	2

Note. Only satellite reflections are included and the intensities given are relative to the strongest, 111, fluorite reflection. $a = 4.688(3)$ Å, $\alpha = 0.3842(2)$, $\Delta 2\theta = 2\theta_{obs} - 2\theta_{calc}$, $\lambda = 1.5406$ Å.

The 3 + 3D Superspace Group and Constrained Atomic Modulation Functions

Modulation functions for 3 + 3D structures are more complex than those for the more common 3 + 1D structures. In the case of a 3D modulation, three additional indexes *mnp* are needed, together with the normal crystallographic indexes *hkl*, for an indexing of the diffraction pattern. The modulation waves do moreover not proceed through the structure only along the *q*-vector directions, here $\langle 100 \rangle$. They may also go in other directions, e.g., $\langle 110 \rangle$ or $\langle 111 \rangle$, by being combinations of two or three *q* vectors. The order of the satellites for a structure with multidimensional modulations is also not straightforward. The satellites can, however, as also the atomic modulation functions (AMFs), be divided into groups as described below.

A determination and parameterization of the AMFs is important for a refinement of the modulation. For the Bi–Cr phase the single-crystal XRD pattern shows in principal three different satellite types, those with *mnp* indices 111, 200, and 220, and it is thus these that are to be considered in a refinement. The strongest are of type 111, but the two other types are clearly observable. Each AMF is a sum of cosine and sine function contributions that are related to

each other by the point-group symmetry for the atom positions. The site symmetry for the atoms and the direction of the modulation wave determine the AMF constraints and limits the number of refineable parameters. For the Bi–Cr phase the satellite reflections with indexes $m + n$, $n + p$, and $m + p \neq 2j$ are systematically absent and the corresponding modulation waves have zero amplitudes. For the centrosymmetric metal site (0, 0, 0), the high point group symmetry $m\bar{3}m$ rules out cosine function contributions for positional AMFs and sine function contributions for occupational AMFs. The O atom site has, on the other hand, the noncentrosymmetric symmetry $\bar{4}3m$, which allows both sine and cosine functions for occupational as well as positional AMFs. The AMFs must furthermore be built up by a closed group of modulation waves; i.e., the amplitudes of symmetry related modulation waves are identical and follow the crystallographic point group symmetry $m\bar{3}m$. Further direction specific restrictions are generated by the symmetry elements valid for the direction in question. The modulation waves can therefore be divided into groups with specific restrictions, e.g., 310 and 620 type modulations have the same restrictions, which are different from those for, e.g., type 111 and 222. The compositional AMF of the metal atoms for types 111, 200, and 220 is described by Eq. [1] below. Refineable amplitudes for the displacive AMF for these orders of modulation are listed in Table 5. For the metal atoms there are in total 6 refinable parameters, 3 occupational and 3 positional, and for the O atoms in total 12, 6 occupational and 6 positional,

$$\delta f_{\mathrm{M}}(v_1, v_2, v_3)/f_{\mathrm{M}}^{\mathrm{av}} = a_{\mathrm{M}(111)} \cdot F_{111} + a_{\mathrm{M}(200)} \cdot F_{200} + a_{\mathrm{M}(220)} \cdot F_{220}, \quad [1]$$

TABLE 5
Refinable Amplitudes of the 3D Positional AMFs for $Bi_{1-x}Cr_xO_{1.5+1.5x}$

			Sin_x	Sin_y	Sin_z	Cos_x	Cos_y	Cos_z
1	1	1	A_{1S}	A_{1S}	A_{1S}	A_{1C}	A_{1C}	A_{1C}
1	1	−1	A_{1S}	A_{1S}	$-A_{1S}$	A_{1C}	A_{1C}	$-A_{1C}$
1	−1	1	A_{1S}	$-A_{1S}$	A_{1S}	A_{1C}	$-A_{1C}$	A_{1C}
−1	1	1	$-A_{1S}$	A_{1S}	A_{1S}	$-A_{1C}$	A_{1C}	A_{1C}
2	0	0	A_{2S}	0	0	A_{2C}	0	0
2	0	0	A_{2S}	0	0	A_{2C}	0	
0	2	0	0	A_{2S}	0	0	A_{2C}	
2	2	0	A_{3S}	A_{3S}	0	A_{3C}	A_{3C}	0
2	0	2	A_{3S}	0	A_{3S}	A_{3C}	0	A_{3C}
0	2	2	0	A_{3S}	A_{3S}	0	A_{3C}	A_{3C}
−2	2	0	$-A_{3S}$	A_{3S}	0	$-A_{3C}$	A_{3C}	0
2	0	−2	A_{3S}	0	$-A_{3S}$	A_{3C}	0	$-A_{3C}$
0	−2	2	0	$-A_{3S}$	A_{3S}	0	$-A_{3C}$	A_{3C}

Note. For O atoms both sine and cosine functions are allowed, but for metal atoms only sine functions.

$$\begin{aligned}
F_{111} = \{&\cos(2\pi[v_1 + v_2 + v_3]) - \cos(2\pi[-v_1 - v_2 + v_3]) \\
&- \cos(2\pi[-v_1 + v_2 - v_3]) \\
&- \cos(2\pi[v_1 - v_2 - v_3])\}, \\
F_{200} = \{&\cos(2\pi[2v_1 + 0v_2 + 0v_3]) \\
&+ \cos(2\pi[0v_1 + 2v_2 + 0v_3]) \\
&+ \cos(2\pi[0v_1 + 0v_2 + 2v_3]), \\
F_{220} = \{&\cos(2\pi[2v_1 + 2v_2 + 0v_3]) \\
&+ \cos(2\pi[2v_1 + 0v_2 + 2v_3]) \\
&+ \cos(2\pi[0v_1 + 2v_2 + 2v_3]) \\
&- \cos(2\pi[-2v_1 + 2v_2 + 0v_3]) \\
&- \cos(2\pi[2v_1 + 0v_2 - 2v_3]) \\
&- \cos(2\pi[0v_1 - 2v_2 + 2v_3])\},
\end{aligned}$$

where $\delta f_{\mathrm{M}}(v_1, v_2, v_3)$ is the function describing the occupational deviation from the average occupation $f_{\mathrm{M}}^{\mathrm{av}}$ and a_{M} is the refinable amplitude of the AMF. Sine functions of the same type have to be added to the AMF described above for the occupational AMF of the oxygen atoms.

Periodic Nodal Surface

Periodic nodal surfaces (PNSs) can be used for illustrating 3D modulations (11) and are especially useful for describing multidimensional compositional modulations. The 111 type of AMF will mainly be discussed here since it is the most prominent one for the Bi–Cr phase. The 111 type compositional AMF, the F_{111} term in Eq. [1], is accordingly set equal to a constant. By changing the value of the constant, different surfaces through the structure are defined which represent different levels of atomic substitution. The surfaces extend in ordinary 3D space but their periodicity is defined by the value of α. By setting the constant equal to zero the surface with no modulation can be illustrated, i.e., the node of the modulation function. The structure is then divided into two interpenetrating channel systems that are separated by this PNS, illustrated in Fig. 5c. The zero surface represents thus the part in the structure where the Bi^{3+} and Cr^{6+} atoms are statistically distributed. On one side of the surface the Bi^{3+} concentration is higher than average and on the other side the Cr^{6+} concentration is higher than average. By changing the value of the constant it is also possible to find the extreme values of the modulation function, which represent points in the structure with the highest Bi^{3+} and Cr^{6+} concentrations, respectively (see Figs. 5d and 5e). It should, however, be noted that the description here is a simplified one and that a complete description would include modulation functions of other orders, e.g., 200 (Fig. 5a) and 220 (Fig. 5b) in different proportions.

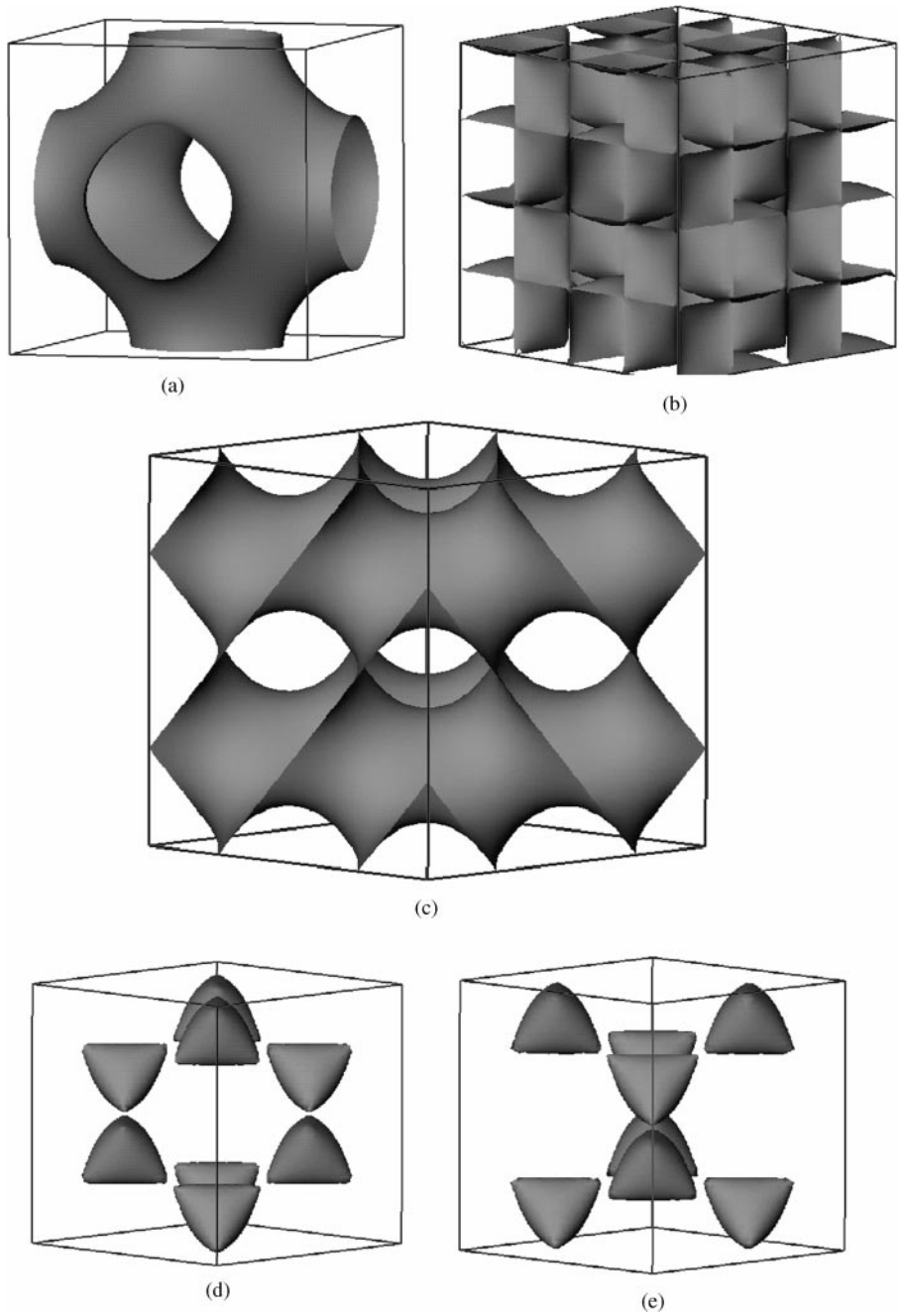

FIG. 5. An illustration of the compositional AMF defined by Eq. [1], with periodic nodal surfaces drawn in the range $-0.5 \leq v_1, v_2, v_3 \leq 0.5$. The compositional AMF of (a) 200 type, (b) 220 type, and (c) 111 type with the constant set equal to zero, and of 111 type with (d) constant = 2 and (e) constant = − 2. The two latter surfaces describe respectively Bi- and Cr-rich parts in the structure.

It is more difficult to describe the displacive modulation function by using a PNS. However, the displacements should follow the compositional changes, there are then no displacement of the atoms on the surface shown in Fig. 5c, and the largest displacements are probably at the areas illustrated in Figs. 5d and 5e.

Optical Spectroscopy

The recorded optical absorption spectra display a strong absorption increase toward the UV region, indicating the existence of broad and very intense absorption features at high energies outside the spectral range measured.

Normalized for absorber thickness, the spectra show that the linear extinction coefficient (α) of the UV-absorption edge is dependent on the degree of Cr-substitution (Fig. 6a). Derivatives of spectra of all three samples display a maximum at 17,400 $\pm$ 150 cm^{-1}. This indicates that the UV edge is caused by a strong absorption peak located at an identical energy in spectra of all three samples. The shift of the UV edge with increasing Cr content is thus caused by an intensification of the UV band, but the position of the band remains constant.

The strong absorption observed in the spectra of the present Cr-doped Bi_2O_3 phases has inferred characteristic features, e.g., energy, intensity, and width, of charge transfer absorption bands. Two main types of electronic transitions to be considered in the present case are ligand to metal (L–M) and metal–metal (M–M) electron transfers. The shift of the UV edge with sample Cr concentration strongly indicates that Cr^{6+} takes part in the absorption process. If the absorption is related to L–Cr^{6+} transfer, the intensity of the band is predicted to display a relation with Cr content (in apfu) as $\alpha = A \cdot (C_{Cr} + C_{Cr}^2)$, where A is the extinction coefficient of the UV band. On the other hand, if a Bi^{3+}–Cr^{6+} charge transfer process operates, the predicted relation between linear extinction coefficient and sample Cr content is $\alpha = A \cdot (C_{Cr} - C_{Cr}^2)$.

Due to the very intense UV absorption it has not been possible to obtain linear extinction data (α-values) at UV-peak maximum. However, provided that the UV-absorption line shape is identical for spectra of all samples, something which is suggested by the derivatives of the measured spectra, comparisons of α-values at arbitary wavenumbers on the absorption edge would provide information suitable for evaluating the actual UV dependence in relation to Cr content. In Fig. 6b, linear extincion coefficients for the three samples at ν = 17,540, 18,020, and 18,520 cm^{-1} are presented as a function of sample Cr-content. Within the present concentration range ($x = 0.15$), any intensity contribution from L–Bi^{3+} charge transfer processes to the UV-edge absorption is predicted to vary at the most by 2% ($\alpha = A \cdot (1.5–1.5 \cdot C_{Cr}^2)$). Consequently, the evolution of the UV-edge absorption will mainly reflect probability variations for the Cr^{6+}-related absorption process. Modeling of the measured linear extinction at the three wavenumbers mentioned using the two α-functions above, and accounting for the predicted variable contribution from L–Bi^{3+} CT, reveal a negligibly higher r^2 value (0.998) for a fit based on a O–Cr charge transfer as the cause for the UV edge than for a fit ($r^2 = 0.994$) to the Bi^{3+}–Cr^{6+} model. The difference in correlation results for the two model fits are smaller than the experimental errors and consequently, the present spectral data can neither confirm nor reject the proposed existence of Bi^{3+}–Cr^{6+} charge transfer processes in Cr-doped Bi-oxides (10).

IR-spectra of powders of the present three Bi–Cr samples (Fig. 7) display a prominent and rather broad absorption band at approximately 840 cm^{-1}, which is assigned to a stretching mode in $Cr^{VI}O_4^{2-}$ tetrahedra (22). An additional shoulder observed at ca 750 cm^{-1} in the recorded spectra is energetically comparable to the bridge stretching modes in dichromates and may be attributed to interactions between anions (23).

Commensurate Approximation

It is difficult to visualize modulated 3 + 3D structures and comparatively straightforward descriptions of them can be obtained by making commensurate approximations. Commensurate approximations are, however, usually very unwise to use for structural refinements. A commensurate structural model for $Bi_{1-x}Cr_xO_{1.5+1.5x}$ with $x \approx 0.05$ is illustrated in Fig. 8a. The model is based on the information at hand about the local environment of Cr^{6+} (Figs. 8b and

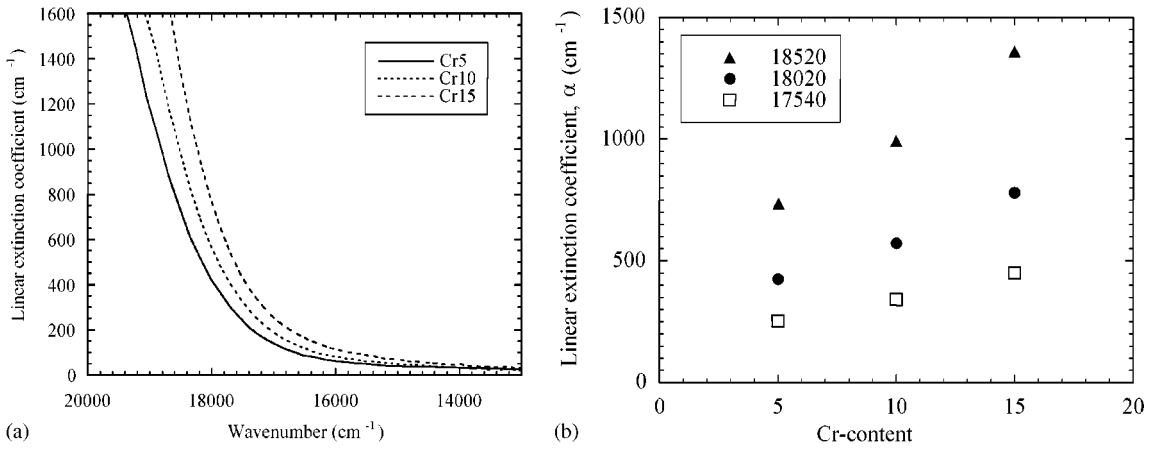

FIG. 6. (a) Optical absorption spectra of $Bi_{1-x}Cr_xO_{1.5+1.5x}$ with $x = 0.05$, 0.10, and 0.15 and (b) the compositional dependency of the linear extinction coefficient at three different wave numbers.

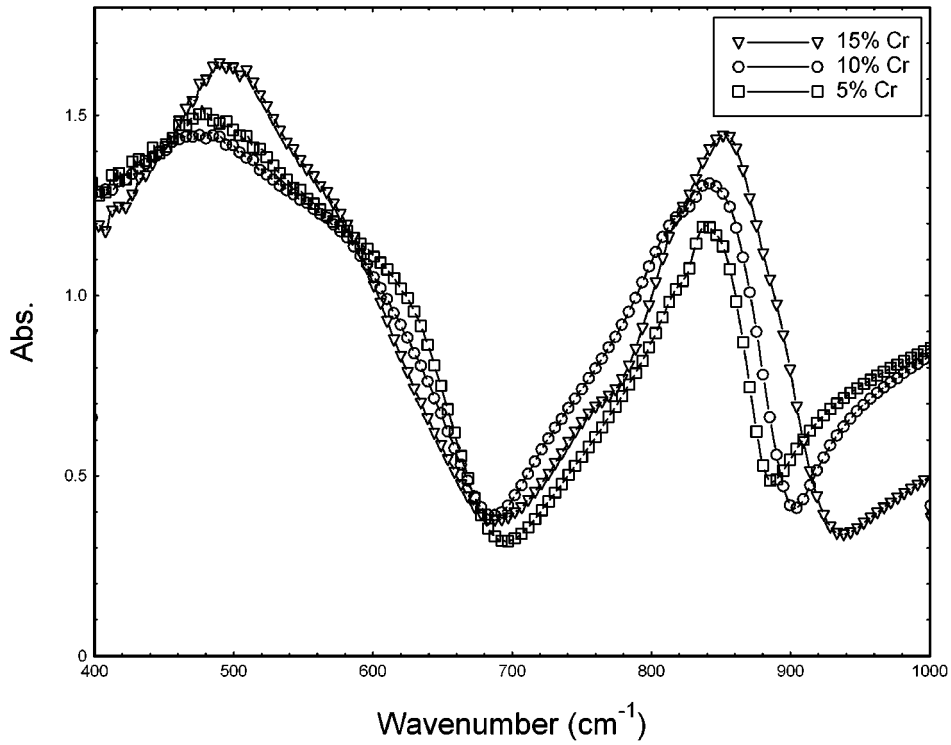

FIG. 7. Infrared spectra of $Bi_{1-x}Cr_xO_{1.5+1.5x}$ with $x = 0.05$, 0.10, and 0.15.

8c) and Bi^{3+} and the modulation vectors, together with the fact that the strongest satellites are of the 111 type. The model is a $3 \times 3 \times 3$ superstructure of a cubic fluorite structure. The noncentrosymmetric space group $F\bar{4}3m$ was used for it in order to enable CrO_4 tetrahedra. A $Fm\bar{3}m$ symmetry would work as well, but with the difference that two interpenetrating, mutually exclusive, O_4 tetrahedra, i.e., a cube, would be formed around each Cr^{6+} ion, each with an occupancy of 50%. The model contains isolated Cr^{6+} ions in the metal matrix at an approximate concentration of 5%. There are no Cr–O–Cr bonds and all neighboring metal atoms to Cr^{6+} are Bi^{3+}, forming $CrBi_{12}$ cuboctahedra.

Cr^{6+} is, because of its small ionic radius (0.40 Å) (24), in almost all known oxides coordinated by four O atoms forming a CrO_4 tetrahedron, while in an ideal fluorite type structure it would be coordinated by 8 O atoms forming a CrO_8 cube. The Bi–Cr phase has, however, an oxygen deficient fluorite structure with O atom vacancies. By removing half of the O atoms from the CrO_8 cube the CrO_4 tetrahedron is formed. Since Cr^{6+} has a much smaller ionic radius than Bi^{3+} (1.17 Å) (24), the Cr^{6+}–O distance should be smaller than that for Bi^{3+}–O and be ca. 1.7 Å. This will lead to a relaxation of the positions of the neighboring Bi and remaining O atoms. Since the oxygen vacancies in the model are around the Cr^{6+} ions, the coordination number for the 12 Bi atoms closest to a Cr atom is 6–7. The relaxation around the tetrahedrally coordinated Cr^{6+} ions is a possible reason for the formation of the modulation wave, being accordingly of both occupational and positional nature.

The structure contains Cr^{6+} centers that order incommensurately with respect to the basic cubic fluorite structure. Most of the oxygen vacancies are then concentrated around these Cr^{6+} centers and the rest of the structure is forced to relax toward or from them. When the Cr concentration is increased in the structure, for $0.05 \leq x \leq 0.15$, the CrO_4 tetrahedra will probably start to build $Cr_2O_7^{2-}$ dichromate clusters, as indicated by the IR spectroscopy data.

DISCUSSION

$Bi_{1-x}Cr_xO_{1.5+1.5x}$ with $0.05 \leq x \leq 0.15$ is an interesting phase from several points of view; the high + VI oxidation state of Cr, the tetrahedral CrO_4 units in the fluorite-type structure, an anticipated high oxygen ion conductivity, and the complex and fundamental crystallographic features, such as the 3D incommensurate modulation. All of these issues and crystal chemical features should and will be studied further. The future investigations will of course profit from a use of single-phase samples and relatively large single crystals as prepared in this work. Ionic conductivity measurements combined with neutron and X-ray

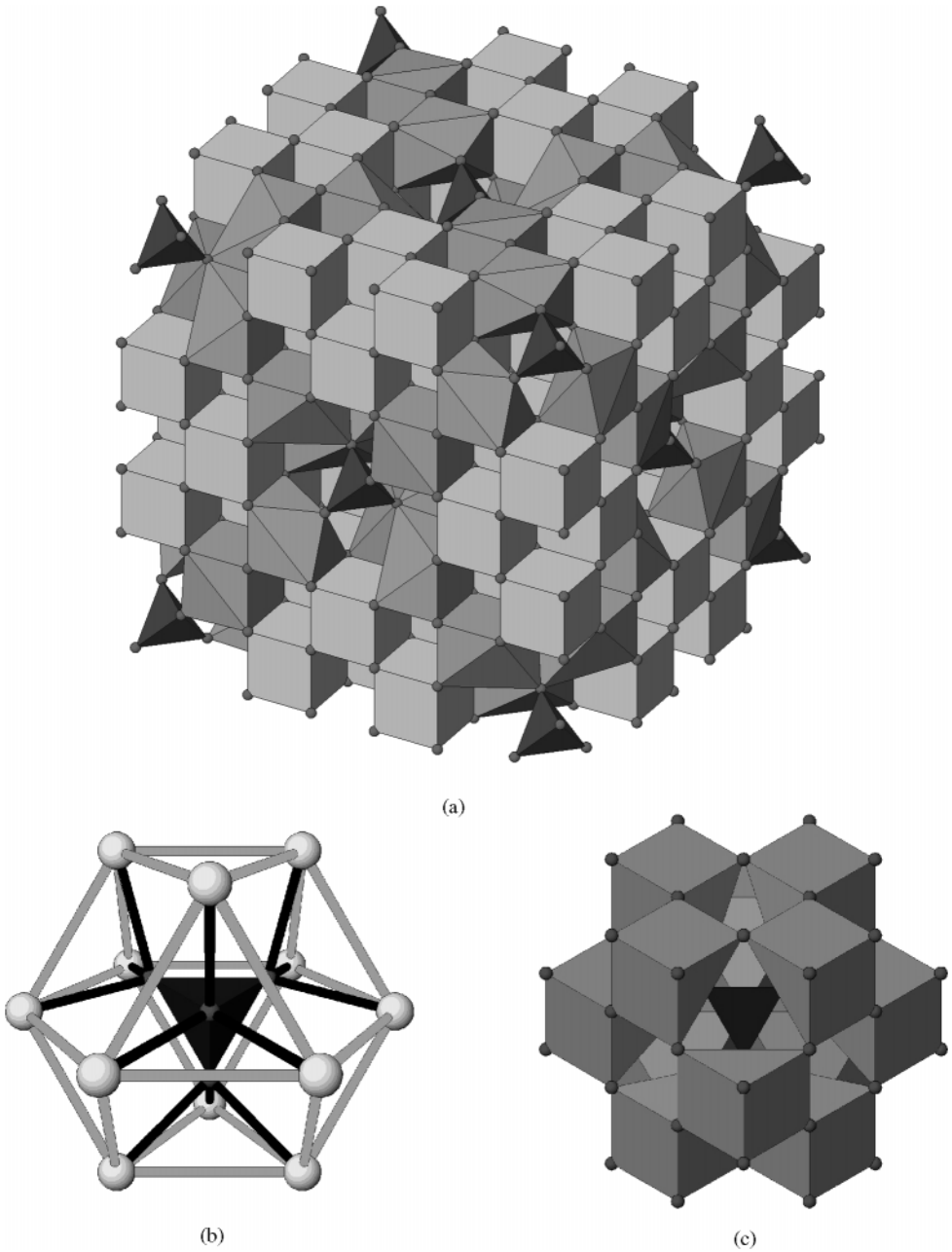

FIG. 8. (a) A polyhedral illustration of a commensurate approximant structure model for $Bi_{1-x}Cr_xO_{1.5+1.5x}$ ($x \approx 0.05$), consisting of a $3 \times 3 \times 3$ superstructure of the average cubic fluorite type structure. (b) The local coordination of Cr^{6+} by 12 Bi atoms forming a cuboctahedron or (c) by 12 BiO_7 units. The model structure is built up by CrO_4 tetrahedra, dark gray BiO_7 polyhedra, and light gray BiO_8 cubes.

diffraction studies, including of the 3D modulation, are in progress.

The structural similarity and differences in symmetry between the title compound and $Bi_{1-x}Nb_xO_{1.5+x}$ with $0.06 < x < 0.23$ have clearly been demonstrated here. It can be noted that the oxygen content in both phases is found to vary between ca. $MO_{1.56}$ and $MO_{1.73}$. Since both compounds are cubic, a natural question is if they are a solid solution of the δ-Bi_2O_3 phase or not. The fact that the phases become less stable at lower dopant contents may indicate a direct phase relation with δ-Bi_2O_3, i.e., that their stability ranges may extend to pure Bi_2O_3, only with an increasing difficulty to quench them to room temperature with decreasing concentrations of the added metal atoms.

Another interesting question is why five, including here the title compound, of all the eight 3D modulated structures reported are found in bismuth oxide systems. $Bi_{1-x}Cr_xO_{1.5-1.5x}$, $0.05 \leq x \leq 0.15$, $Bi_{0.84}Mo_{0.16}O_{1.74}$ (7), Bi_{1-x}

$Nb_xO_{1.5+x}$, $0.06 < x < 0.23$, and $Bi_{1-x}Ta_xO_{1.5+x}$, $0.1 < x < 0.25$ (3, 11), with average fluorite-type structures, and $BaBi_3O_{5.5}$ (12,13) possessing an average bcc type metal ordering. This question is yet to be answered, but it surely shows the structural complexity of bismuth oxide-based compounds.

ACKNOWLEDGMENTS

The authors thank Prof. S. Lidin and Dr. P. Berastegui for valuable discussions. This work has been financially supported by the Swedish Natural Science Council NFR.

REFERENCES

1. D. J. Boivin and G. Mairesse, *Chem. Mater.* **10,** 2870 (1998).
2. A. Castro, E. Aguado, J. M. Rojo, P. Herrero, R. Enjalbert, and J. Galy, *Mater. Res. Bull.* **33**(1), 31 (1998).
3. C. D. Ling, R. L. Withers, S. Schmid, and J. G. Thompson, *J. Solid State Chem.* **137,** 42 (1998).
4. W. Zhou, *J. Solid State Chem.* **108,** 381 (1994).
5. C. E. Infante, C. Gronemeyer, and F. Li, *Solid State Ionics* **25,** 63 (1987).
6. K. Sooryanarayana, R. Somashekar, and T. N. Guru Row, *Solid State Ionics* **104,** 319 (1997).
7. M. Valldor, S. Esmaeilzadeh, C. Pay-Gomez, and J. Grins, *J. Solid State Chem.* **152,** 573 (2000).
8. W. Zhou, *J. Solid State Chem.* **87,** 44 (1990).
9. W. Zhou, *J. Solid State Chem.* **101,** 1 (1992).
10. S. A. Warda, W. Pietzuch, W. Massa, U. Kesper, and D. Reinen, *J. Solid State Chem.* **149,** 209 (2000).
11. R. L. Withers, C. D. Ling, and S. Schmid, *Z. Kristallogr.* **214,** 296 (1999).
12. C. Michel, D. Pelloquin, M. Hervieu, B. Raveau, F. Abbattista, and M. Vallino, *J. Solid State Chem.* **109,** 122 (1994).
13. S. Esmaeilzadeh, P. Berastegui, J. Grins, and H. Rundlöf, *J. Solid State Chem.* **152,** 435 (2000).
14. A. Yamamoto, *Acta Crystallogr. B* **38,** 1451 (1982).
15. R. L. Withers, Y. C. Feng, and G. H. Lu, *J. Phys. Condens. Matter* **2,** 3187 (1990).
16. M. Ohmasa, K. Hagiya, K. Tomeoka, and A. Ueda, *in* "Aperiodic '94" (G. Chapius and W. Paciorek, Eds.), pp. 475–477. World Scientific, Singapore, 1995.
17. S. Hovmöller, *Ultramicroscopy* **41,** 121 (1992).
18. K. E. Johansson, T. Palm, and P.-E. Werner, *J. Phys. E* **13,** 1289 (1980).
19. P. D. Battle, C. R. A. Catlow, J. Drennan, and A. D. Murray, *J. Phys. C* **16,** 561 (1983).
20. "Winfit beta release, 1.2.1." S. Krumm, Institut für Geologie, Erlangen, Germany, 1997.
21. P. D. Battle, C. R. A. Catlow, J. W. Heap, and L. M. Moroney, *J. Solid State Chem.* **63,** 8 (1986).
22. K. Nakamoto, "Infrared and Raman Spectra of Inorganic and Coordination Compounds," 5th ed., part A. Wiley, New York, 1997.
23. J. A. Campbell, *Spectrochimica Acta* **21,** 1333 (1965).
24. R. D. Shannon, *Acta Crystallogr. A* **32,** 258 (1965).